

Simulation of flow over an inclined spheroid at high Reynolds number: tripping effects

M. Plasseraud¹, P. Kumar¹, R. Ma¹ and K. Mahesh¹

(¹Department of Aerospace Engineering and Mechanics, University of Minnesota, USA)

ABSTRACT

The modeling of trip-induced laminar-to-turbulent boundary layer transition and turbulent near-wall flow over an inclined prolate spheroid is challenging due to high Reynolds number, three-dimensionality of the boundary layer and the rapidly varying pressure gradient on the body. Tripping such a flow is non-trivial and a compromise has to be reached between adding enough perturbation to trigger transition over a range of pressure gradients while keeping the downstream flow free from trip-specific features. Large eddy simulation is used to study this problem to assist the planning of experiments as part of ONR's HIPRO program. The influence of trip location is first studied using wall-modeled large eddy simulation (WMLES). The boundary layer is axisymmetrically tripped and the flow resulting from three different tripping locations is compared. Wall-resolved and trip-resolved LES (WRLES) is then performed to assess the effects of cylindrical post trips under experimental consideration. The physical details of how a single trip element causes transition is studied using global linear stability analysis of a laminar boundary layer tripped by a cubical element. The global stability analysis is able to capture the frequency of the primary vortical structures observed in nonlinear direct numerical simulation (DNS). The results show that the varicose unstable mode extracts its energy from both the wall-normal and spanwise shear of the central low-speed streak, and its instability core is located within the reversed flow region downstream of the cube. A preliminary study of alternative trip configurations is performed for three different canonical geometries: cylindrical post, wire and delta wing. Results show that the trip geometry has an influence on the type of perturbation that is introduced, which in turn affects the effectiveness of the tripping in term of downstream distance at which the boundary layer becomes turbulent.

INTRODUCTION

The flow around a 6:1 prolate spheroid at angle of attack is a canonical problem that shows many similarities with the flow observed around complex, real-world submerged bodies. Despite the simplicity of the geometry, the resulting flow is complex and exhibits a three-dimensional boundary layer evolving under a streamwise varying pressure gradient, cross-flow separation and reattachment. The pressure gradient varies azimuthally, from favorable on the windward side, to adverse on the leeward side. This drives the near-wall flow along the side of the spheroid, resulting in separation and formation of a pair of counter-rotating vortices. The vortex pair entrains surrounding flow and reattaches the boundary layer towards the leeward centerline.

In practice, the flow is tripped at model scale to attain high Reynolds number behavior, and ensure that the transition to turbulence is repeatable, although the best approach to do so remains unclear. Difficulties arise when designing an effective trip to successfully trigger flow transition over a range of angles of attack and Reynolds numbers, without significant history effects post-tripping. In particular, finding an appropriate location to trip the flow is non-trivial. While an early trip is desirable so that a larger portion of the boundary layer is fully turbulent, it is also harder to achieve because the local Reynolds number is smaller. In the case of the flow around the prolate spheroid, earlier tripping faces the additional constraint that the windward favorable pressure gradient is stronger hence more prone to under-tripping while the leeward adverse pressure gradient is also larger and more likely to overtrip. In addition, the choice of trip geometry can be challenging; e.g. Erm and Joubert (1991) who studied a zero pressure gradient flow over a flat plate tripped using distributed roughness grit, cylindrical pins and wire. Different geometries trigger different modes of perturbation which translate into different evolution of the boundary layer to a turbulent state.

Global linear stability theory (Theofilis, 2011) can provide insight into the early stages of temporal disturbance growth in a tripped boundary layer and is especially useful for non-parallel flows such as roughness wakes. It is therefore a promising tool to predict and analyze the tripping effects. Isolated, three-dimensional roughness elements may be considered as the primary models to be generalized and extended for more complex trip geometries. Loiseau et al. (2014) used global stability theory to investigate the flow past a cylindrical roughness element. They suggested that the frequencies associated with the dominant fluid dynamics are well predicted by global stability analyses, and that the unstable nature of the central low-speed streak is of crucial importance in the transition process. Bucci et al. (2021) noted that the roughness Reynolds number and aspect ratio might not be the only important parameters for transition characteristics, the shear ratio also plays a crucial role in the onset and symmetry of the primary global instability. The joint effects of these parameters make the instability characteristics and transition process highly sensitive to the flow configuration. In this paper, we perform global linear stability analysis to gain insight in the unstable nature induced by a cube immersed in a laminar boundary layer.

The present work is focused on boundary layer tripping in context of flow over the spheroid. The objectives of this study are: (i) to compare the influence of trip location on turbulent flow around the prolate spheroid; (ii) to assess the sensitivity of the tripping effectiveness to geometry of the trip. The numerical approach is discussed in the next section, followed by a detailed problem description and discussion of results. Finally, the key outcomes of the present work are summarized.

NUMERICAL APPROACH

The LES solves the filtered incompressible Navier–Stokes equations using the algorithm developed by Mahesh et al. (2004) for unstructured grids on massively parallel platforms. The spatially-filtered incompressible Navier–Stokes equation are:

$$\frac{\partial \bar{u}_i}{\partial t} + \frac{\partial}{\partial x_j} (\bar{u}_i \bar{u}_j) = -\frac{\partial \bar{p}}{\partial x_i} + \nu \frac{\partial^2 \bar{u}_i}{\partial x_j \partial x_j} - \frac{\partial \tau_{ij}}{\partial x_j} \quad (1)$$

$$\frac{\partial \bar{u}_i}{\partial x_i} = 0 \quad (2)$$

where u_i is the velocity, p is the pressure and ν is the kinematic viscosity. The overbar $(\bar{\cdot})$ denotes spatial filtering and $\tau_{ij} = \bar{u}_i \bar{u}_j - \bar{u}_i \bar{u}_j$ is the subgrid stress, which is modeled using the dynamic Smagorinsky model (Germano et al., 1991; Lilly, 1992).

The algorithm uses a finite volume method where the Cartesian velocity components and pressure

are stored at the centroids of the control volumes, while the face normal velocities are stored independently at the centroids of the faces. Time marching is performed using an implicit Crank–Nicolson scheme. The equations are discretized in space with a second order central scheme.

For the wall-modeled LES, the grid resolution requirement near wall is relaxed by employing wall model to account for unresolved near-wall scales. This is achieved by replacing the usual no-slip boundary condition at the wall with a prescribed mean shear stress (τ_w), obtained by assuming that the instantaneous wall-parallel velocity (U) satisfies Reichardt’s law-of-the-wall (Reichardt, 1951) given by:

$$U^+ = \frac{1}{\kappa} \ln(1 + \kappa y^+) + \left(C - \frac{1}{\kappa} \ln \kappa \right) \left(1 - e^{-y^+/11} - \frac{y^+}{11} e^{-y^+/3} \right) \quad (3)$$

where, the superscript ‘+’ denotes normalization using viscous units, and $C = 4.1$ and $\kappa = 0.38$ are constants. Reichardt’s law is chosen as it is valid for the entire inner layer, as opposed to the log-law which only holds for $y^+ > 50$ or so. This ensure accuracy and robustness as the boundary layer thickness can vary a lot over the body. For a given $u = U$ at a wall-normal location $y = d$, Eq. (3) is solved using the Newton–Raphson method to obtain $\tau_w = u_\tau^2$, which is then prescribed at the wall by setting the face velocity to zero and the eddy viscosity (ν_t) as:

$$\nu_t = \tau_w d / U - \nu \quad (4)$$

where, ν is the kinematic viscosity. This implementation of wall model was found more robust compared to setting $\nu_t = 0$ and modifying wall face velocity to prescribe τ_w .

For the resolved trip geometry studies, the trips were resolved using the incompressible LES overset methodology developed by Horne and Mahesh (2019a,b). This methodology enables a large degree of freedom in the grid generation process.

The global stability analysis linearizes the incompressible Navier–Stokes equations about a base state, U_b and describes the evolution of a small perturbation \tilde{u}_i and \tilde{p} .

$$\frac{\partial \tilde{u}_i}{\partial t} + \frac{\partial}{\partial x_j} (\tilde{u}_i U_{b,j}) + \frac{\partial}{\partial x_j} (U_{b,i} \tilde{u}_j) = -\frac{\partial \tilde{p}}{\partial x_i} + \nu \frac{\partial^2 \tilde{u}_i}{\partial x_j \partial x_j},$$

$$\frac{\partial \tilde{u}_i}{\partial x_i} = 0. \quad (5)$$

An encapsulated formulation of the selective frequency damping (SFD) method developed by Jordi et al. (2014) is used to obtain the stationary base flow. The main idea is to apply a temporal low-pass filter to damp the oscillations due to the unsteady part of the solutions, and is achieved by introducing a linear forcing term on the right-hand side of the Navier–Stokes equations. The problem is

considered to have converged when $\|q - \bar{q}\|_{inf} \leq 10^{-8}$ according to Jordi et al. (2014), where \bar{q} is the filtered state. The base flow for the present case converges over a time period of $T = 1000h/U_e$.

The numerical schemes used to solve the Linearized Navier-Stokes (LNS) equations are identical to that used to obtain the base state (Mahesh et al., 2004). A matrix-free method - the implicitly restarted Arnoldi method (IRAM) is implemented in the PARPACK library to solve for the leading eigenvalues and eigenmodes. A temporal exponential transformation of the eigenvalue spectrum is performed. The eigenvalue problem is integrated over time $\tau = 0.9$ and converges over 227 iterations. Also, Adjoint sensitivity analysis is performed that solves for the dominant eigenvalues and eigenmodes of the adjoint LNS Equations. The adjoint perturbation velocity field highlights optimal locations for point forcing and the inception of instability (Hill, 1995). The continuous adjoint equations are:

$$\begin{aligned} \frac{\partial \tilde{u}_i^\dagger}{\partial t} + \frac{\partial}{\partial x_j} (\tilde{u}_i^\dagger U_{b,j}) - \tilde{u}_j^\dagger \frac{\partial}{\partial x_i} U_{b,j} &= -\frac{\partial \tilde{p}^\dagger}{\partial x_i} - v \frac{\partial^2 \tilde{u}_i^\dagger}{\partial x_j \partial x_j}, \\ \frac{\partial \tilde{u}_i^\dagger}{\partial x_i} &= 0. \end{aligned} \quad (6)$$

PROBLEM DESCRIPTION

WMLES of the flow around a prolate spheroid

WMLES of the flow around the spheroid is performed at 2.5 and 15 degrees angle of attack and $Re = 6.5 \times 10^6$. The flow is numerically tripped at $x/L = 0.05$, $x/L = 0.10$ and $x/L = 0.20$ by prescribing a azimuthally uniform steady wall-normal blowing. The location of the $x/L = 0.20$ numerical trip is identical to the reference experiments of Chesnakas and Simpson (1996) and is commonly used by past experiments. The wall-normal blowing strategy has been validated for the flow over the Suboff hull at 0° angle of attack (Kumar and Mahesh (2018); Morse and Mahesh (2021)).

The computational grid contains 3 million hexahedral cells to enable fast turn around and a qualitative assessment of tripping effects. A longitudinal view of the grid is shown in Figure 1. The computational domain is a cylinder of length $36a$ in the major axis of the spheroid and radius of $16a$ where a is the length of semi-minor axis of the spheroid.

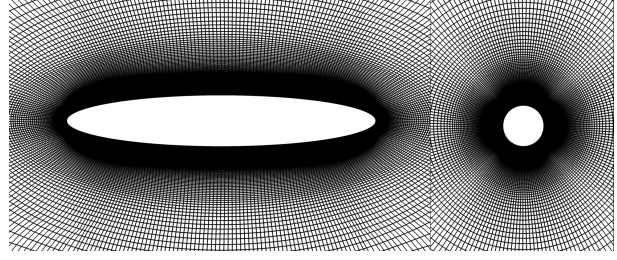


Figure 1: Longitudinal view of the 3M prolate spheroid grid.

The coordinate system and the domain are aligned with respect to the spheroid. A uniform velocity is prescribed at the inflow plane. The freestream is inclined to match the angle of attack. The usual no-slip boundary condition at the wall is replaced by a prescribed wall stress obtained using the aforementioned wall model. The simulations are advanced in time with a non-dimensional time step $\Delta t U/a = 0.004$, where U is the freestream velocity magnitude. The simulations are performed for at least two flow-through time to discard transients and then for another few flow-through times sampled at every five time steps to obtain time-averaged flow field.

Trip-resolved LES of the flow around the prolate spheroid

WRLES is performed on the prolate spheroid at 0° and 20° angles of attack, at $Re = 4.2 \times 10^6$. Both the boundary layer and the trip geometry are resolved in order to study the effect by which the boundary layer transitions to turbulence. The grid is composed of 600 million unstructured hexahedral elements. The trip geometry and location is identical to the preliminary design from the HIPRO campaign. It consists of 20 azimuthally distributed cylindrical posts which have an aspect ratio $h/d = 5 : 2$ where $h = 5 \times 10^{-3}L$ is the height of the post and $d = 2 \times 10^{-3}L$ is its diameter. The trips are located at $x/L = 0.067$. Each post has its separate overset mesh, which promotes reusability, allows for additional flexibility in the grid generation process and improves grid quality and efficiency overall. Though the boundary layer has non-uniform thickness due to the pressure gradient, the ratio h/δ_{99} , where δ_{99} is the boundary layer thickness, is estimated to vary between 5/1.4 on the windward side to 5/7 on the leeward side, with a Reynolds number based on δ_{99} around 2000.

Global stability analysis

The global stability and sensitivity analyses of flow over an isolated cubic roughness element is performed at different Re_h in a range of 450-600. The flow configuration, computational domain and roughness geometry are depicted in figure 2. The cuboid with height h and width d is centered at the origin of the Cartesian coordinate system. The cubes with equal length and width are considered because they can provide similar global stability results as cylindrical posts. The ratio of the roughness height to the displacement thickness of the boundary layer h/δ^* is 2.86, which is large and related to an early trip location. While a trip at an early location is desirable to obtain a turbulent boundary layer over a large portion of the body, it is also harder to achieve since the local Reynolds number is smaller. The present case aims to provide insight into how moving a trip closer to the leading edge affects the transition. The aspect ratio $\eta = d/h = 1$. This case is denoted by Case $(Re_h, \eta) = (600, 1)$. The roughness height is $h = 1$, the reference length in the simulations. The streamwise extent of the computational box L_x is $45h$. The spanwise extent is $L_z = 10h$ to ensure that the roughness element behaves as isolated, and the wall-normal extent is $L_y = 15h$. The distance from the inlet of the computational domain to the center of the roughness element is denoted by $l = 15h$. The Blasius laminar boundary layer solution is specified at the inflow boundary, and convective boundary conditions are used at the outflow boundary. Periodic boundary conditions are used in the spanwise direction. No-slip boundary conditions are imposed on the flat plate and the roughness surfaces. The boundary conditions $U_e = 1$, $\partial v/\partial y = \partial w/\partial y = 0$ are used at the upper boundary. Uniform grids are used in the streamwise and spanwise directions, and the grid in the wall-normal direction is clustered near the flat plate.

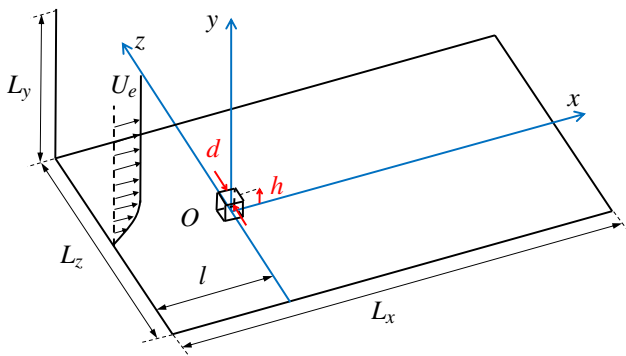


Figure 2: Sketch of the flow configuration and roughness geometry.

Alternative trip geometries

The flow around three different trip geometries on a no-slip flat plate is computed using LES. Three different trip geometries are considered: a cylindrical post with a 1:1 height to diameter aspect ratio, where the height of the post h is unit; a unit-diameter cylindrical wire; a “delta wing”, which is an equilateral triangle at 40 degree angle of attack, whose centroid is at $y = 1.5h$ where $h = 1$, the length of the base of the triangle. The grid used for the delta trip is shown in Figure 3. The support of this trip was not modeled. The angle of attack was chosen such that a large separation occurs on the leeward side and produce a counter-rotating vortex pair that perturbs the boundary layer. The inflow is set as a Blasius velocity profile with a boundary layer thickness $\delta_{99} = 1.5h$, which was chosen to be similar to the expected conditions on the prolate spheroid study and the location of the trip. No pressure gradient is imposed. The Reynolds number based on trip height is prescribed as $Re_h = U_e h / \nu = 1000$, where U_e is the boundary layer edge velocity and h is the roughness height, which corresponds to $\delta^* = 522$.

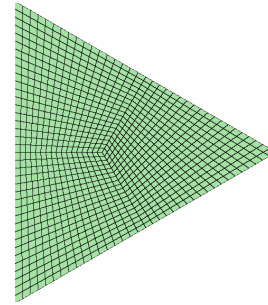


Figure 3: Grid of the delta trip

RESULTS AND DISCUSSION

WMLES of the flow around a prolate spheroid

Figure 4 shows the averaged streamwise velocity on the center plane along with the near-wall streamlines at 2.5° and 15° angle of attack. The streamlines are constrained to the first cell and are equivalent to friction lines. At 2.5° , the flow is close to being axisymmetric and does not form a vortex pair. Two stagnation points are observed at the nose and at the tail, close to the major axis of the prolate spheroid. Away from the wall, the flow is accelerated to be maximum in a region extending from the trip until about $x/L = 0.8$ to $x/L = 0.9$. This acceleration is consistent with the favorable pressure gradient that exists on the foremost half of the prolate spheroid. The fact that velocity increases more strongly past the trip, away from the wall, is likely due to a reduction of the skin friction associated with the transition of the boundary layer turbulence at this location. Near the wall on the other hand, the velocity is maximum at the nose upstream of the trip, then drops to a minimum directly downstream of the trip. The near-wall velocity is then slowly re-accelerated until the aft part of the spheroid. The near-wall streamlines are at a slight angle with respect to the major axis of the prolate spheroid. No convergence line is observed which suggests that no boundary layer separation exists.

At 15° , the flow is not axisymmetric. A stagnation point is seen at the nose, slightly windward. Two higher velocity regions are observed at the higher incidence on the windward side in the aft-most half of the spheroid and on the leeward side on the fore-most half of the prolate spheroid. The windward centerline constitutes a stagnation line. From there, the flow splits on each side of the prolate spheroid and travels predominantly in the streamwise direction.

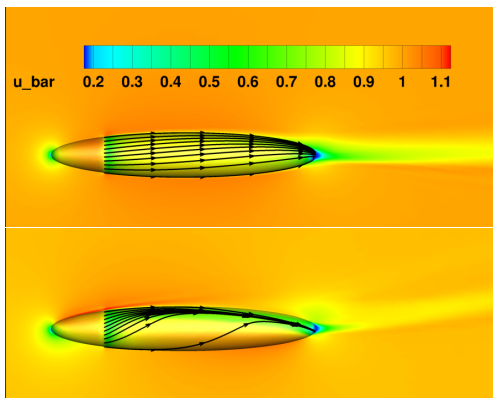


Figure 4: Averaged streamwise velocity at 2.5° and 15° angles of attack. The flow is tripped at $x/L = 0.2$

The azimuthal component of velocity increases to reach a maximum around $\phi = 90^\circ$, which is observed as an inflection of the streamline curvature.

The streamlines converge on the leeward side, which indicates the primary boundary layer separation resulting in the formation of the primary vortex. On the other hand, the leeward centerline at $\phi = 180^\circ$ corresponds to a divergence of the streamlines associated with the reattachment of the flow from the primary vortex pair.

Figures 5 to 8 show the skin friction coefficient C_f and pressure coefficient C_p along the streamwise coordinate x/L , at 2.5° and 15° of incidence respectively, at three locations on the spheroid: on the windward side ($\phi = 0^\circ$), on the port side ($\phi = 90^\circ$) and on the leeward side ($\phi = 180^\circ$). Each line represent at different tripping location.

Similar trends are observed for both incidences and at the three locations considered. First, the boundary layer is laminar and C_f decreases from the leading edge to the location of the trip. The skin friction rises to peak around $0.08x/L$ downstream of the trip. Since the boundary layer is turbulent, C_f decreases until it flattens at the midsection. Finally, the skin friction rises again in the aft portion of the spheroid to drop sharply downstream of $x/L = 0.9$, where the flow separates at the tail.

Two regions are identified in the evolution of C_f . Directly downstream of the trip, the three curves do not overlap. This region is understood as a trip dependent area where the value of skin friction is affected by the signature of the trip. Farther downstream, the curve eventually collapse into a single value. This is interpreted as a trip-independent region where the boundary layer has erased the signature of the trip. The challenge of effective tripping is to reach the latter region as early as possible so that the measured flow is independent of the trip.

At 2.5° incidence, similar behaviors are seen for the three azimuthal stations since the flow is near-axisymmetric. In reference to the $0.05x/L$ tripping, the value of skin friction coefficient from the spheroid tripped at $0.10x/L$ collapses much faster to the one from the spheroid tripped at $0.05x/L$ than the one tripped at $0.20x/L$. The reason for that may be that the pressure gradient is weaker at $0.20x/L$ as seen in Figure 7, hence the trip behaves differently than the other two cases and the boundary layer takes longer to transition to a canonical, trip-independent turbulent state.

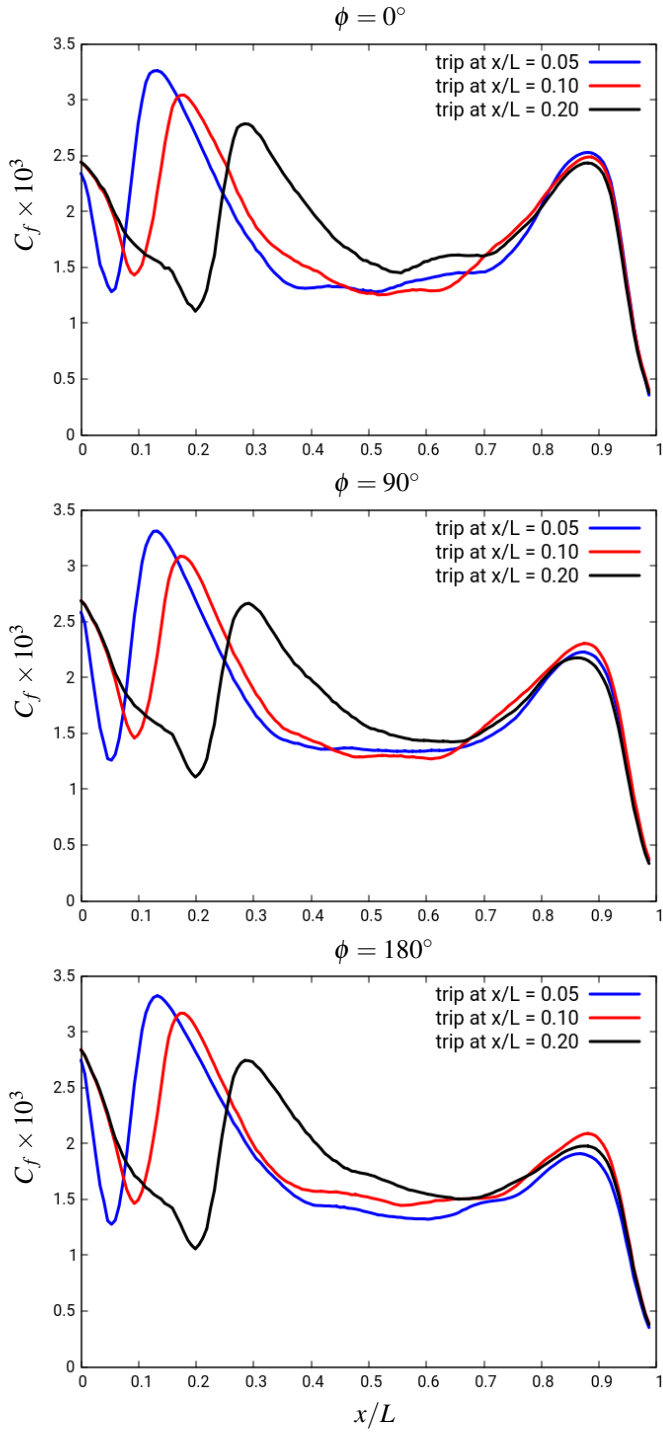


Figure 5: Skin friction coefficient along the prolate spheroid at 2.5° angle of attack, at $\phi = 0^\circ$ (top plot), $\phi = 90^\circ$ (middle plot) and $\phi = 180^\circ$ (bottom plot).

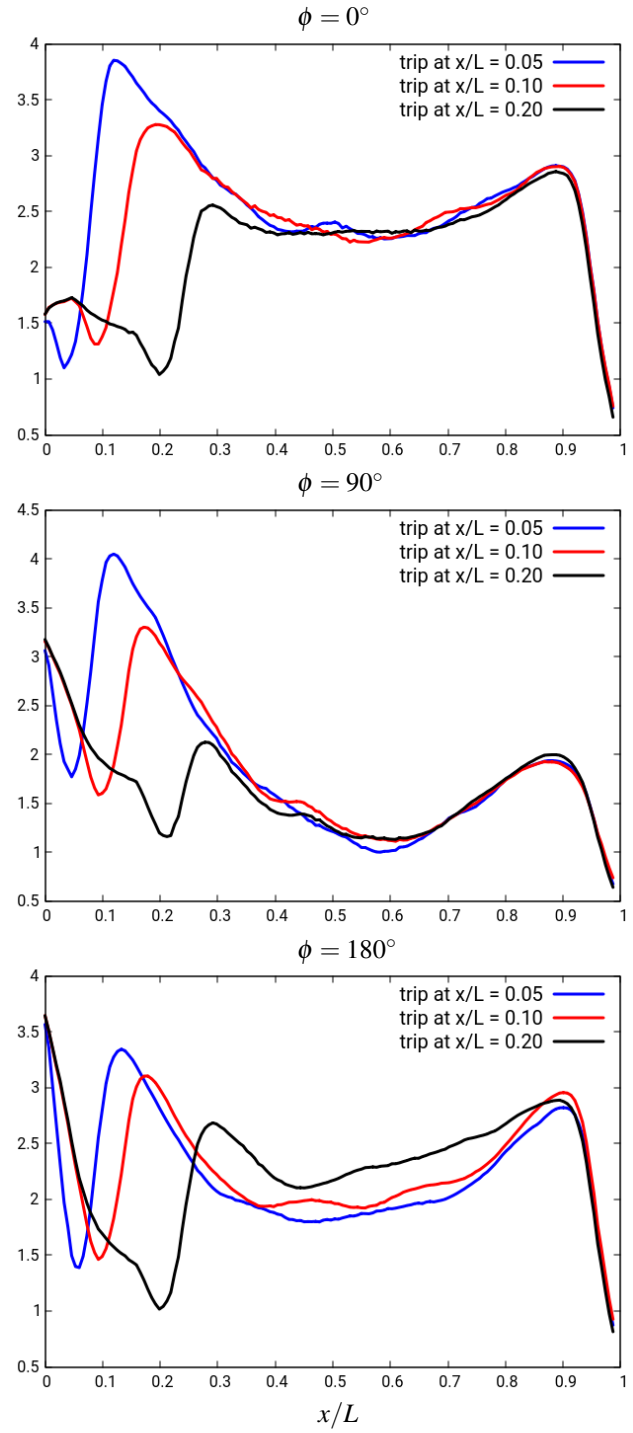


Figure 6: Skin friction coefficient along the prolate spheroid at 15° angle of attack, at $\phi = 0^\circ$ (top plot), $\phi = 90^\circ$ (middle plot) and $\phi = 180^\circ$ (bottom plot).

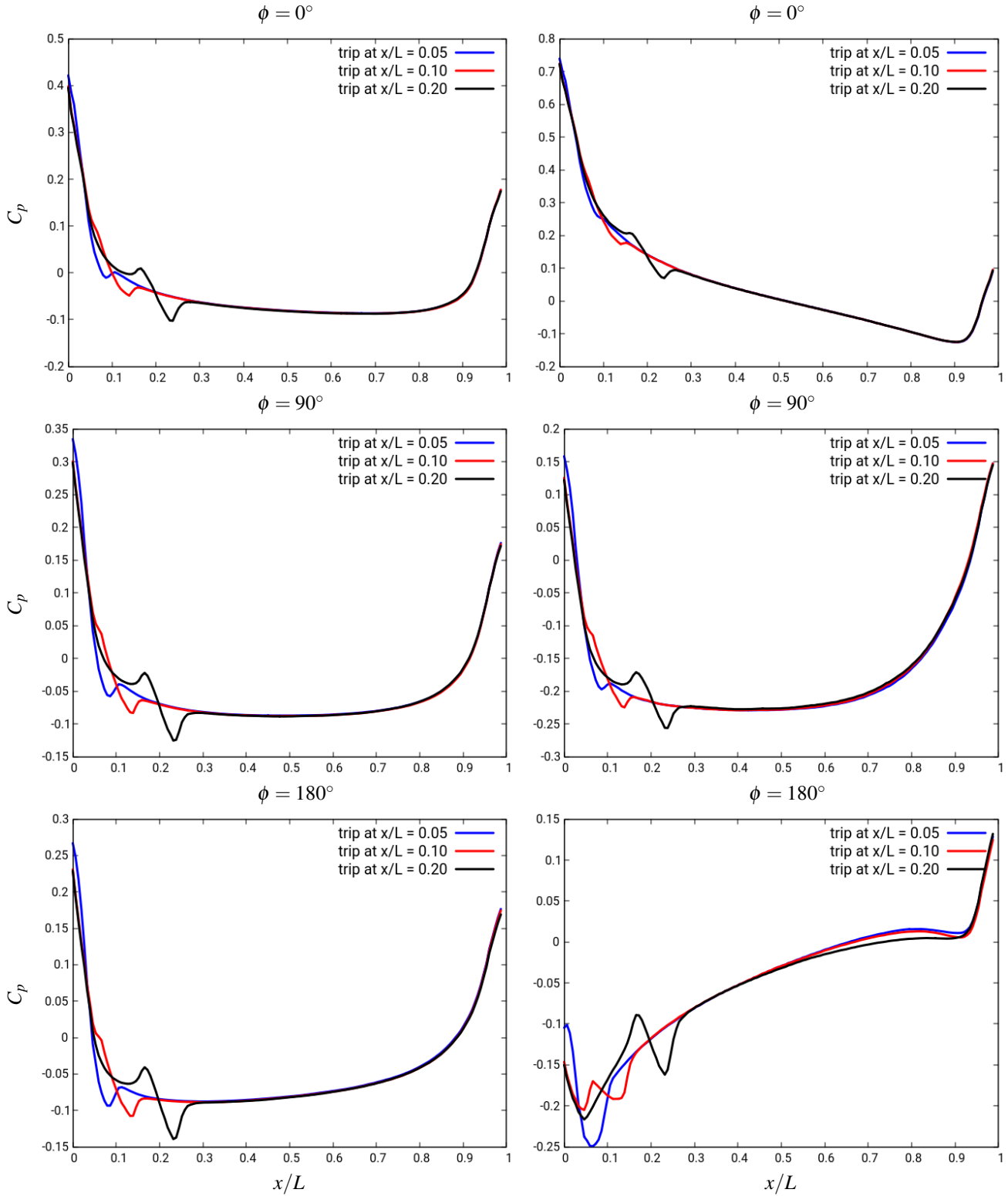


Figure 7: Pressure coefficient along the prolate spheroid at 2.5° angle of attack, at $\phi = 0^\circ$ (top plot), $\phi = 90^\circ$ (middle plot) and $\phi = 180^\circ$ (bottom plot).

Figure 8: Pressure coefficient along the prolate spheroid at 15° angle of attack, at $\phi = 0^\circ$ (top plot), $\phi = 90^\circ$ (middle plot) and $\phi = 180^\circ$ (bottom plot).

At 15° , the $0.20x/L$ curves collapse with the other two shortly after the rise in C_f for the $\phi = 0^\circ$ and $\phi = 90^\circ$ cases, when the pressure gradient is favorable though no obvious collapse is visible until $x/L = 0.9$ at $\phi = 180^\circ$ where the pressure gradient is adverse. The $0.10x/L$ curve collapses with the $0.05x/L$ case quickly at all three azimuthal positions on the other hand. Similarly to the 2.5° case, it is possible that a stronger difference of pressure gradient at the $0.20x/L$ compared to the $0.10x/L$ might explain these observations. In addition, conversely to the $\phi = 0^\circ$ and $\phi = 90^\circ$ stations, the $\phi = 180^\circ$ is located on the leeward centerline, which is the location at which the primary vortex pair reattaches onto the body. One could expect that the value of skin friction along this line is affected by the structure of the vortex pair which itself depends on the turbulent state of the boundary layer prior to separation. A laminar boundary layer would separate earlier which would create a larger vortex and a different value of C_f at the reattachment line. By this mechanism, it is possible that small difference in the location of the trip could translate into larger deviations in the skin friction on the leeward side.

Overall, for both angles of attack, placing the trips at $0.05x/L$ and $0.10x/L$ seems to yields a shorter trip-dependent region hence a more effective tripping. The skin friction coefficient is sensitive on the location of the trip at low angle of attack, and at high angle of the attack on the leeward centerline.

Trip-resolved LES around the prolate spheroid

Figure 9 shows the flow directly downstream of the trip at 0° angle of attack, which is subject to a weak favorable pressure gradient. The posts are effective in introducing unsteadiness in the flow and the boundary layer becomes transitional. The velocity profiles downstream of the trip, behind and between posts are given in Figure 10. The shape of both profiles evolves to display a linear section in the semi-logarithmic scale starting at around $x/L = 0.20$. This suggests that the flow evolves from a transitional state to a turbulent flow around $0.13x/L$ downstream of the trip. The profiles between the two streamwise stations are different at $x/L = 0.10$, which can be understood by the fact that the perturbation introduced by the post is initially local in the spanwise direction. Both stations then converge to a similar profile at $x/L = 0.20$ which indicates that the boundary layer becomes statistically axisymmetric. Both these observations suggest that this trip becomes effective within $0.13x/L$ downstream of the posts at 0° angle of attack.

Figure 11 shows the skin friction coefficient on the port side and on the windward side of the nose of the prolate spheroid at 20° angle of attack.

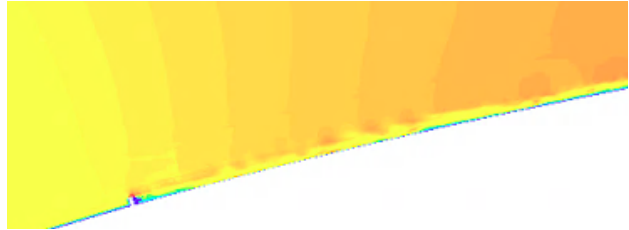


Figure 9: Flow field around the resolved trip on the prolate spheroid at 0° angle of attack.

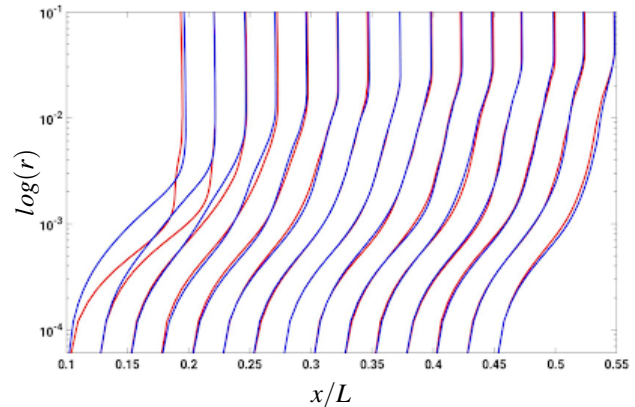


Figure 10: Averaged velocity profiles downstream the trips, directly behind the post (red) and between two posts (blue) at 0° angle of attack.

The perturbation introduced by the posts is visible as streaks which are convected from the windward side to the leeward side at an angle larger than the incidence of the flow. This is assumed to be a consequence of the centrifugal balance inside the boundary layer: a slower moving fluid follows a larger curvature, which is along the ϕ direction on the prolate spheroid. A strong asymmetry is observed between a quiescent windward side and an unsteady leeward side where the perturbation from all the post except one located at $\phi = 0^\circ$, converges. The wake originating from the latter post remains in the centerline though the skin friction diminishes rapidly. Despite the perturbation of this post, an area of low skin friction is seen where the boundary layer flow is steady. Figure 12 gives the evolution of the velocity profile directly behind the $\phi = 0^\circ$ post and adjacent to it, between the trips. Both sets have different shapes closer to the post at $x/L = 0.10$, which converge toward a similar profile at around $x/L = 0.30$. This difference in the profiles is thought to be a consequence of the localized, wake-like perturbation introduced by the trip in which the flow downstream is more unsteady than on the side. This wake-like structure also visible in the skin friction on Figure 11. The profiles remain laminar throughout with a slight increase

in boundary layer thickness. The absence of transition is thought to be related to the quiescent area observed in the skin friction and is understood as a consequence of a stabilizing favorable pressure gradient which dampens the excitation of the post, with a strong crossflow which advects the perturbed flow away from the windward side.

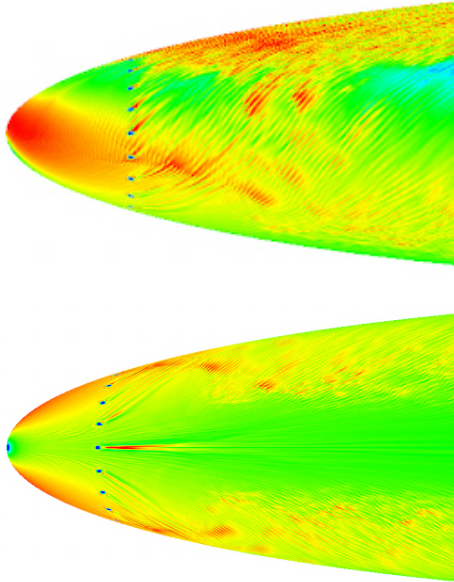


Figure 11: Skin friction at the nose of the prolate spheroid at 20° angle of attack on the port side (top) and on the windward side (bottom).

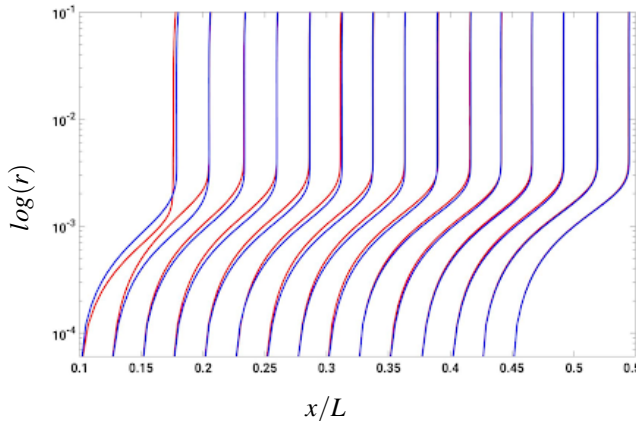


Figure 12: Averaged velocity profiles downstream the windward trip, directly behind the post (red) and between two posts (blue) at 20° angle of attack.

Global instability and adjoint sensitivity analyses

How does a single trip element induce transition? Recall the problem formulation depicted in figure 2; the

base flow computed using SFD method is examined in figure 13. The isosurfaces of the streamwise velocity deviation $u_d = U_b - u_{bl}$ are used to visualize the high- and low-speed streaks. The central low-speed streak which originates from the flow separation downstream of the roughness element, is symmetric with respect to the mid-plane. The lateral low-speed streaks are associated with the counter-rotating vortices. High-speed streaks appear farther downstream and are attached to the wall.

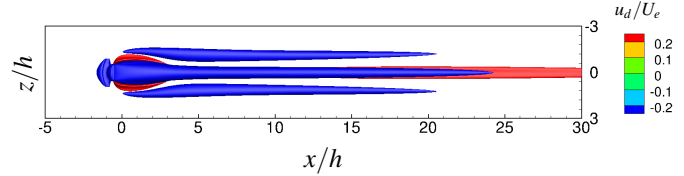


Figure 13: Top view of high- and low-speed streaks, visualized by isosurfaces of the streamwise velocity deviation of the base flow from the Blasius boundary layer solution, $u_d = U_b - u_{bl}$, for Case $(Re_h, \eta) = (600, 1)$.

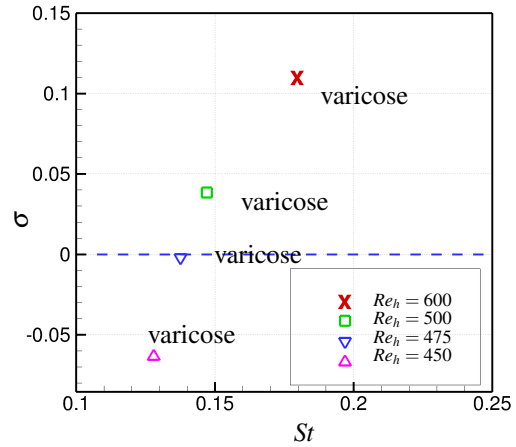


Figure 14: Leading eigenvalues of cases with $\eta = 1$ at different Re_h .

Global stability analysis was performed at different Re_h , and the leading eigenvalues are shown in figure 14. At each Re_h , one leading eigenvalue is obtained. The changeover from an unstable to a stable system typically occurs when the Reynolds number exceeds a certain threshold. The case at $Re_h = 450$ is absolutely stable, consistent with the steady flow field observed from the DNS results. As Re_h increases, both the growth rate and the temporal frequency are increased. The critical Re_h of global instability can be identified when the growth rate of an eigenvalue becomes positive for the first time. The flow at $Re_h = 475$ is marginally stable which suggests that

the critical Re_h is close to 475 for this configuration. The eigenfrequency from linear stability analysis is consistent with the Strouhal number of hairpin vortices ($St = 0.175$ at $Re_h = 600$).

All the eigenmodes of the leading eigenvalues show varicose symmetry for the various Re_h investigated, where varicose symmetry means a symmetric mode shape with respect to the spanwise mid-plane. The other mode type, the sinuous mode, presents anti-symmetry and is expected to occur for a thinner trip geometry and a higher Reynolds number (Ma and Mahesh, 2021). The real part of the leading eigenmodes is shown for $Re_h = 600$ in Figure 15. The shape and location of the mode correspond to those of the central low-speed streak observed in Figure 13.

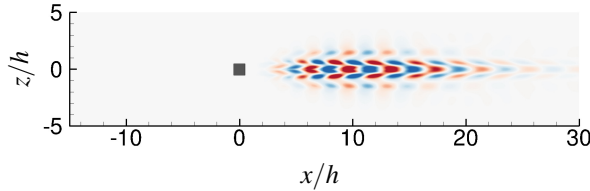


Figure 15: Contour plots at slice $y = 0.5h$ of the streamwise velocity component of the leading unstable global mode for Case $(Re_h, \eta) = (600, 1)$. The contour levels depict $\pm 10\%$ of the mode's maximum streamwise velocity.

The production of disturbance kinetic energy provides insight into how the global mode extracts its energy from the base flow. As illustrated by De Tullio et al. (2013) and Loiseau et al. (2014), the main contributions to the production of disturbance kinetic energy are the two terms

$$P_y = -|\hat{u}||\hat{v}|\frac{\partial U_b}{\partial y}, P_z = -|\hat{u}||\hat{w}|\frac{\partial U_b}{\partial z}. \quad (7)$$

The streamwise variation and spatial distribution of these two dominant terms are examined for Case $(Re_h, \eta) = (600, 1)$ in Figure 16. In combination with the production terms, the local shear is visualized by the solid contour lines of $u_s = ((\partial U_b / \partial y)^2 + (\partial U_b / \partial z)^2)^{1/2}$ in Figure 16, where U_b is the streamwise velocity of the base flow. The distributions of P_y and P_z show a coincidence with the location of the streaks, indicating that the varicose mode extracts the energy from the wall-normal and spanwise shear of the base flow. These results confirm that the varicose mode demonstrates the instability of the entire 3-D shear layer.

The adjoint perturbation velocity field highlights the most receptive regions to momentum forcing, which

provides important information on the regions to trip the flow. The leading adjoint eigenvalues and the results show good agreement with their associated direct eigenmode counterpart. The streamwise velocity component of the leading adjoint modes is depicted in Figure 17. The adjoint modes are located immediately upstream of the roughness element as well as on the top edge of the separation region directly above and downstream of the roughness element. The adjoint mode shows varicose symmetry with respect to the spanwise mid-plane, corresponding to the direct varicose mode.

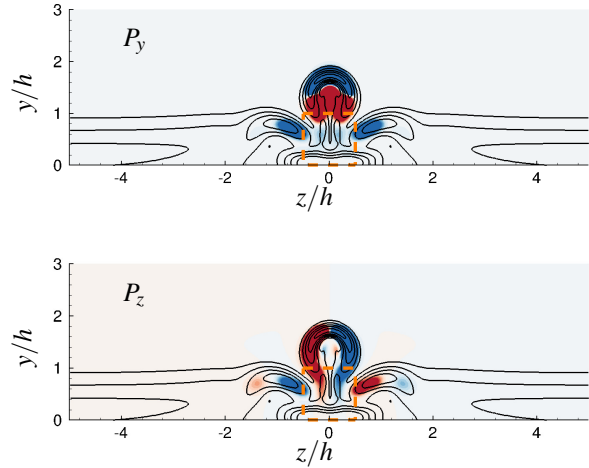


Figure 16: Contours of P_y on the left and P_z on the right in cross-flow planes at $x = 10h$ for Case $(Re_h, \eta) = (600, 1)$. The contour levels are shown within the range from $-1.0e^{-7}$ (blue) to $1.0e^{-7}$ (red). The localized shear is depicted by the solid lines of $u_s = ((\partial U_b / \partial y)^2 + (\partial U_b / \partial z)^2)^{1/2}$ from 0 to 2. The orange dashed lines show the location of the element.

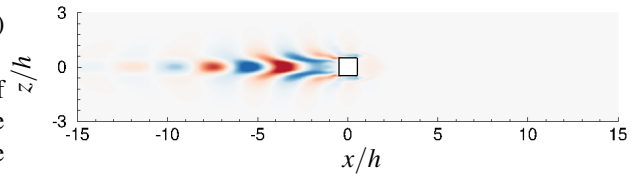


Figure 17: Contour plot of the leading adjoint varicose mode for Case $(Re_h, \eta) = (600, 1)$.

Due to the non-normality of the global linear evolution operator, neither direct nor adjoint solution alone can describe the whole picture. The product for each j th pair of direct and adjoint global modes computed as

$$W_j(x, y, z) = \frac{||\hat{u}^j|| ||\hat{u}^{\dagger, j}||}{\max(||\hat{u}^j|| ||\hat{u}^{\dagger, j}||)}, \quad (8)$$

determines the region where the eigenvalues of the linearized Navier–Stokes operator are most sensitive to localized feedback (Giannetti and Luchini, 2007), - also called the "wavemaker" regions. Locations where $W \approx 1$ are sensitive to localized feedback, corresponding to the instability core. The value of W can be interpreted as quantification of a possible change in the eigenvalues as a result of applied forcing in the given region of the flow (Ilak et al., 2012).

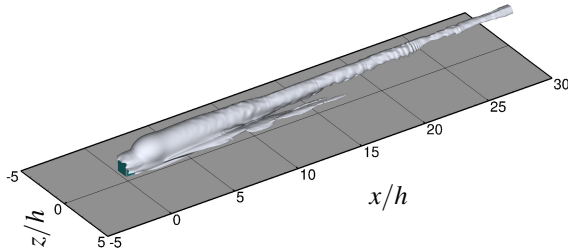


Figure 18: Isosurfaces of the wavemaker for the leading varicose mode in Case $(Re_h, \eta)=(600, 1)$.

Figure 18 depicts the wavemaker regions for the leading mode of Cases $(Re_h, \eta)=(600, 1)$. The wavemaker for the varicose mode is prominent on the top edge of the reversed flow region and over an extended region along the central low-speed streak. The wavemaker has its maximum value within the separation region, and drops to the order of 10^{-1} as it passes through the reversed flow region. This indicates that the global varicose instability has its core in the reversed flow region, and is associated with a convective nature of the shear layer which can aid the formation of hairpin vortices farther downstream.

Canonical trip study

Preliminary results of the flow around the three trip geometries displayed in Figure 19 indicate that the three obstacles trigger different modes of perturbation. The delta wing produces streamwise counter-rotating wingtip vortices whose orientation is controlled by the angle of attack. A positive angle of attack yields a clockwise - counter-clockwise (CW-CCW) pair which entrains the flow from the outer region of the boundary layer to the wall. Conversely, a negative angle of attack creates a CCW-CW vortex pair which lifts the flow from the wall to the unperturbed region. This vortex pair eventually breaks down and perturbs the flow. The angle of attack could be used to provide control over the transition of the boundary layer. The cylindrical post produces a streamwise CCW-CW vortex pair, similarly to the delta trip at a negative angle of attack. In addition, the post produces a wake-like structure, visible as a low momentum region downstream of the trip, between the

vortex pair and down to the wall. Conversely to the delta and the post, the wire generates a large (over 10h) spanwise recirculation bubble. This stationary vortex eventually sheds downstream into streamwise vortices.

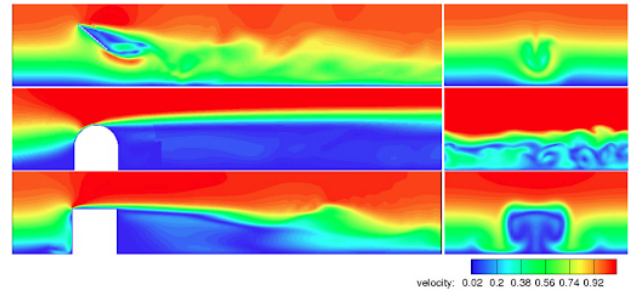


Figure 19: Velocity magnitude in the longitudinal (left) and transverse (right) slices. From top to bottom: delta wing, wire, cylindrical post.

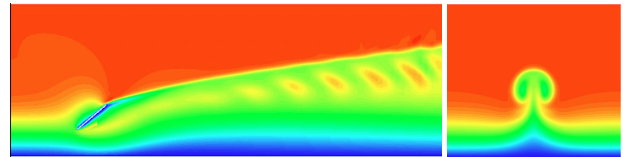


Figure 20: Velocity magnitude in the longitudinal (left) and transverse (right) slices for the delta wing trip at $AoA = -40^\circ$. See legend on Figure 19.

Figure 20 shows the velocity field downstream of the delta trip at a negative angle of attack $AoA = -40^\circ$. Similarly to the delta trip at positive angle of attack, two counter-rotating vortices are produced through the lift of the geometry, although the pair rotates in the opposite direction since the direction of the lift is opposite. The vortex pair is lifted up, away from the wall as the streamwise coordinate is increased. These vortices also produce entrainment region at the centerplane of the domain which was not observed in the three flows of Figure 19. This entrainment region lifts the low-momentum fluid from the near-wall region. Some perturbation is visible between the vortex pair.

Though both the delta post at negative angle of attack and the cylindrical post result in the formation of a CCW-CW pair, little resemblance is observed between the two flows. While the downstream flow from the delta is dominated by the vortex pair, the flow downstream of the post has lower momentum, no entrainment zone and constant wall-normal position of the vortices.

Future simulations will consider longer domains to allow the development of a turbulent boundary layer, and examine the far-field impact of these different near-field perturbations.

SUMMARY

The flow around a 6:1 prolate spheroid is simulated using WMLES at $Re = 6.5 \times 10^6$ and 2.5° and 15° angles of attack for three trip locations. The variation of the skin friction coefficient along the spheroid is used as a metric to evaluate the sensitivity of the flow to the location of the tripping. It is found that having a trip at $x/L = 0.20$ yields a trip-dependent region which extends farther downstream than having a trip at $x/L = 0.05$ and $x/L = 0.10$.

The performance of a trip consisting of 20 cylindrical posts was assessed with wall-resolved and trip-resolved large-eddy simulation at $Re = 4.2 \times 10^6$. At 0° angle of attack, the boundary layer is found to transition to a statistically axisymmetric turbulent state within $0.13x/L$ of the trips. At 20° , the crossflow advects the perturbation created by the windward side posts, to the leeward side. This effect combined with the strong favorable gradient are proposed to explain the presence of a quiescent, laminar area on the windward side of the prolate spheroid, downstream of the trips.

Global stability and adjoint sensitivity analyses are performed for a cubic roughness element immersed in a laminar boundary layer at a relatively large shear ratio $h/\delta^* = 2.86$. The results suggest that the critical Re_h for instability is 475. The varicose global mode is observed in both the subcritical and supercritical regimes. The varicose instability has its root in the center of the reversed flow region, experiences spatial transient growth along the central low-speed streak and extracts its energy from the whole 3-D shear layer, contributing to the birth of hairpin vortices. As the global unstable mode diminishes farther downstream, the hairpin vortices break down and the nonlinear saturation becomes strong.

In addition, the behavior of a cylindrical post, a delta geometry and a cylindrical wire trips are studied at $Re_h = 1000$. The wire introduces a recirculation bubble which sheds downstream, while both the post and the delta trips create a streamwise vortex pair. In the latter case, the direction and intensity of the vortex pair is dictated by the angle of attack of the obstacle. Distinctly different near-field perturbations are observed whose far-field impact will be examined in future studies.

ACKNOWLEDGEMENTS

This work is supported by the United States Office of Naval Research under ONR Grant N00014-20-1-2717 with Dr. Peter Chang as technical monitor. Computing resources are provided by the Engineer Research and Development Center through the High Performance Computing Modernization Program, the Texas Advanced Computing Center through the Extreme Science and Engineering Discovery Environment allocation and the Minnesota Supercomputing Institute.

REFERENCES

- Bucci, M. A., Cherubini, S., Loiseau, J. C., and Robinet, J. C. "Influence of freestream turbulence on the flow over a wall roughness". *Physical Review Fluids*, 6(6): 063903, 2021.
- Chesnakas, C. J. and Simpson, R. L. "A detailed investigation of the 3d separation about a 6:1 prolate spheroid at angle of attack". *AIAA Journal*, 96(0320), 1996.
- De Tullio, N., Paredes, P., Sandham, N. D., and Theofilis, V. "Laminar-turbulent transition induced by a discrete roughness element in a supersonic boundary layer". *Journal of Fluid Mechanics*, 735:613-646, 2013.
- Erm, L. P. and Joubert, P. N. "Low-Reynolds-number turbulent boundary layers". *Journal of Fluid Mechanics*, 230:1-44, 1991.
- Germano, M., Piomelli, U., Moin, P., and Cabot, W. H. "A dynamic subgrid-scale eddy viscosity model". *Physics of Fluids A*, 3:7:1760, 1991.
- Giannetti, F. and Luchini, P. "Structural sensitivity of the first instability of the cylinder wake". *Journal of Fluid Mechanics*, 581:167-197, 2007.
- Hill, D. C. "Adjoint systems and their role in the receptivity problem for boundary layers". *Journal of Fluid Mechanics*, 292:183-204, 1995.
- Horne, W. J. and Mahesh, K. "A massively-parallel, unstructured overset method for mesh connectivity". *Journal of Computational Physics*, 376:585-596, 2019a.
- Horne, W. J. and Mahesh, K. "A massively-parallel, unstructured overset method to simulate moving bodies in turbulent flows". *Journal of Computational Physics*, 397(108790), 2019b.
- Ilak, M., Schlatter, P., Bagheri, S.n, and Henningson, D. S. "Bifurcation and stability analysis of a jet in cross-flow: onset of global instability at a low velocity ratio". *Journal of Fluid Mechanics*, 696:94-121, 2012.
- Jordi, B. E., Cotter, C. J., and Sherwin, S. J. "Encapsulated formulation of the selective frequency damping method". *Phys. Fluids*, 26(3):034101, 2014.
- Kumar, P. and Mahesh, K. "Large-eddy simulation of flow over an axisymmetric body of revolution". *Journal of Fluid Mechanics*, 853:537-563, 2018.
- Lilly, D. K. "A proposed modification of the Germano subgrid-scale closure model". *Physics of Fluids A*, 4:3: 633, 1992.

- Loiseau, J. C., Robinet, J. C., Cherubini, S., and Leriche, E. “Investigation of the roughness-induced transition: global stability analyses and direct numerical simulations”. Journal of Fluid Mechanics, 760:175–211, 2014.
- Ma, R. and Mahesh, K. “Global stability analysis and direct numerical simulation of boundary layers with an isolated roughness element”. arXiv preprint arXiv:2112.02708, 2021.
- Mahesh, K., Constantinescu, G., and Moin, P. “A numerical method for large-eddy simulation in complex geometries”. Journal of Computational Physics, 197:1:215–240, 2004.
- Morse, Nicholas and Mahesh, Krishnan. “Large-eddy simulation and streamline coordinate analysis of flow over an axisymmetric hull”. Journal of Fluid Mechanics, 926, 2021.
- Reichardt, H. “Vollständige darstellung der turbulenten geschwindigkeitsverteilung in glatten leitungen”. ZAMM-Journal of Applied Mathematics and Mechanics/Zeitschrift für Angewandte Mathematik und Mechanik, 31(7):208–219, 1951.
- Theofilis, V. “Global linear instability”. Annual Review of Fluid Mechanics, 43:319–352, 2011.

DISCUSSION COMMENTS

David R. Dowling, University of Michigan.

This interesting paper describes the impact of boundary trip placement and angle of attack on boundary layer tripping results for a six-to-one prolate spheroid at Reynolds numbers of 6.5 and 4.2 million at various angles of attack. Additional results for the global stability of flow past a single cubical roughness element, and for different trip geometries are also provided. The paper is well written and the various computational tasks are clearly defined.

- In Fig. 6, I am surprised that the skin friction coefficient, C_f , is at $x/L = 0.90$ is nearly the same on both the windward side ($\alpha = 0^\circ$) and the leeward side ($\alpha = 180^\circ$) for the 15° angle of attack. I expected to be higher on the windward side as it is for the 2.5° angle of attack. Thus, I would like to know: does the definition of C_f in this manuscript utilize the local flow speed or the upstream flow speed? Or, what phenomena leads to the high at the aft end of the prolate spheroid at the 15° angle of attack?*
- Fig. 11 nicely illustrates the geometrical difficulty associated with tripping the flow over this model at non-trivial angles of attack. However, it would be nice to know why the 'patchy' red regions occur and what causes the striations (most clearly seen in the upper panel of Fig. 11). Are the Fig. 11 images, 'time-averaged' or 'snapshot-in-time' results? Does the 'patchiness' of the skin-friction results also occur at other flow conditions?*
- And finally, even though the authors suggest otherwise, I am struck by the unexpected visual likeness of the wakes of the cylindrical post (bottom panels of Fig. 19) and the delta wing at a negative angle of attack (Fig. 20). The primary visual differences are the stronger wake velocity deficit from the post and the greater lifting of the vortices downstream of the wing. Do these two elements perform similarly as boundary layer trip devices? I am interested in this because the post's performance should not depend on the incoming boundary layer flow's direction across the surface (a nice feature for experiments) while that of delta wing will likely depend on the wing's yaw angle with respect to the incoming flow.*

RESPONSE TO DISCUSSION COMMENTS

We thank the referee for the comments and questions. Please find below the Authors' responses.

- The skin friction coefficient is defined based on the freestream velocity. On the aft windward side, the increase in the skin friction is understood to be related to the acceleration of the flow at this location (see Figure 4). It is unclear why the aft peak of skin friction is similar magnitude in both angle of attacks.
- Figure 11 shows the instantaneous skin friction. These patches are instantaneous and have been observed to be a transitional, intermittent feature. The Authors' hypothesis is that the striations are the consequence of crossflow instabilities at this location, which manifests itself as spanwise oscillation of the main component of velocity. The striations have been observed on other, finer grids although it is unclear if they appear at other angles of attack or Reynolds number.
- Indeed, both the post and the delta produce a counter-rotating vortex pair in the wake although the mechanism of inception is different (i.e. horse-shoe vortex in the case of the post, generation of lift in the case of the delta) and as noted, the loss of momentum is higher in for the former. The effectiveness of the trips is currently being studied quantitatively. As commented, one advantage of the post is invariance in yaw however the higher loss of momentum may cause over-tripping. One advantage of the delta is that it offers additional degrees of freedom to modulate the strength of the perturbation through the angle of attack.